Multicolor 3D Super-resolution Imaging by Quantum Dot Stochastic Optical Reconstruction Microscopy

Jianquan Xu,[†] Kayvan F. Tehrani, and Peter Kner*

College of Engineering, University of Georgia, Athens, Georgia 30602, United States. [†]Present address: University of Pittsburgh Cancer Institute, Research Pavilion, HCCLB 2.35, 5117 Centre Avenue, Pittsburgh, PA 15232.

ABSTRACT We demonstrate multicolor three-dimensional super-resolution imaging with quantum dots (QSTORM). By combining quantum dot asynchronous spectral blueing with stochastic optical reconstruction microscopy and adaptive optics, we achieve three-dimensional imaging with 24 nm lateral and 37 nm axial resolution. By pairing two short-pass filters with two appropriate quantum dots, we are able to image single blueing quantum dots on two channels simultaneously, enabling multicolor imaging with high photon counts.

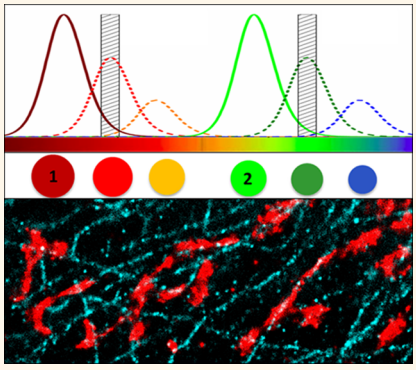

KEYWORDS: fluorescence microscopy · quantum dots · super-resolution microscopy · stochastic optical reconstruction microscopy

Several super-resolution imaging techniques have been developed that allow the diffraction-limited resolution to be surpassed,[1,2] including stimulated emission depletion (STED) microscopy,[3,4] structured illumination microscopy (SIM),[5] stochastic optical reconstruction microscopy (STORM),[6] and photoactivatable localization microscopy (PALM).[7] These techniques can be classified into two categories: (i) those which spatially modulate the fluorescence emission with patterned illumination (STED, SIM) and (ii) those which stochastically switch individual molecules on at different times (STORM, PALM). The second category takes advantages of single-molecule localization,[8] using photoswitching or another mechanism to stochastically turn on only a small fraction of the fluorophores in the field of view. Such individual molecules can then be localized to an accuracy of $\sim s/\sqrt{N}$, where s is the width of the point spread function (PSF) and N is the number of collected photons. Images with sub-diffraction-limited resolution are then reconstructed from the measured positions of individual fluorophores by imaging sparse subsets of molecules over many cycles.

Quantum dots (QDs) have shown promise for biological imaging due to their remarkable photostability and brightness.[9−11] In particular, QDs show great promise for super-resolution fluorescence microscopy. The fluorescence of Mn-doped ZnSe nanocrystals can be modulated with greater than 90% efficiency through reverble excited-state absorption, and ZnSe QDs have been used to achieve a 4.4-fold increase in resolution over the diffraction limit using the RESOLFT (reversible saturable or switchable optical fluorescence transitions) technique.[12] QDs have also been used with 4Pi microscopy to achieve 100 nm axial resolution.[13] CdSe QDs have been used to enhance spatial resolution by exploiting their natural blinking or enhanced blinking properties with super-resolution optical fluctuation imaging (SOFI).[14,15] In the technique quantum dot blinking with three-dimensional imaging (QDB3), 3D super-resolution imaging with blinking QDs is achieved by extracting the PSF of individual QDs by subtracting subsequent frames, again exploiting the stochastic blinking of the QDs.[16] However,

* Address correspondence to kner@engr.uga.edu.

Received for review December 5, 2014 and accepted February 21, 2015.

Published online February 22, 2015
10.1021/nn506952g

compared to other photoswitchable probes, QDs spend a rather short time in the off state, limiting the number of QDs that can be distinguished within the area of a PSF, thereby making it difficult to exploit the natural QD blinking for single-molecule super-resolution imaging. For STORM, it is necessary that the off-time of each molecule is much greater than the on-time.

To address this problem, a blueing technique has been developed that makes QDs suitable for use in STORM imaging.[17] In solutions containing oxygen, the fluorescence emission of QDs is observed to shift stochastically to shorter wavelengths. By observing the QD fluorescence emission with a band-pass filter at a shorter wavelength than the QD initial fluorescence spectrum, fluorescence from individual QDs can be measured as their emission wavelength stochastically enters the filter passband. Such blueing is attributed to the continuous size reduction of the CdSe core due to photo-oxidation, which is accompanied by a blue shift of the emission wavelength.[18−21]

Compared to the conventional switchable dyes, such as the cyanine dyes, which typically require two different lasers for bleaching and reactivation and a thiol-containing agent to enhance photoswitching, QDs do not need to be bleached; only a single laser is required for excitation of multiple emission wavelength QDs, and no external chemicals are needed. Additionally, for conventional switchable dyes, each dye molecule can photoactivate multiple times, which, on one hand, can enhance the signal, but on the other hand, also allows each probe molecule to sample different locations of the structure in different camera frames and to contribute multiple independent localizations which may result in a potential motion blurring.[22] QD blueing will only localize each molecule once and, because QDs are intensely bright, can still provide enough photons for accurate localization.

Although multicolor imaging has been achieved by many of the super-resolution techniques, such as SIM,[23] STED,[24] PALM,[25,26] and STORM,[27,28] multicolor super-resolution imaging by QDs remains a challenging task. While techniques that rely on QD blinking can be straightforwardly extended to multiple colors, these techniques are not comparable to PALM or STORM in either the resolution that can be achieved or the feasible labeling density. QDs have been used for multiparticle tracking, but these approaches rely on there being only a few QDs in any PSF area and are not easily extended to super-resolution.[29,30]

Here we demonstrate multicolor and 3D super-resolution imaging by QD blueing STORM combined with AO (QSTORM). To enable multicolor imaging, we introduce two QDs in the visible and NIR and two appropriate band-pass filters to image the oxidized visible and NIR QDs, respectively. We demonstrate that, by optimizing the excitation laser intensity and the mounting medium, we can adjust the blueing rate for optimal imaging. We show that the QDs exhibit up to an 80 nm blue shift (longer than previously reported[19]) without overlap between the channels. We further make a detailed comparison between STORM with Alexa dyes and with QDs, demonstrating higher photon counts with QDs. We measure greater than 3000 photons per localization from QDs and measure a microtubule width of 46 nm.

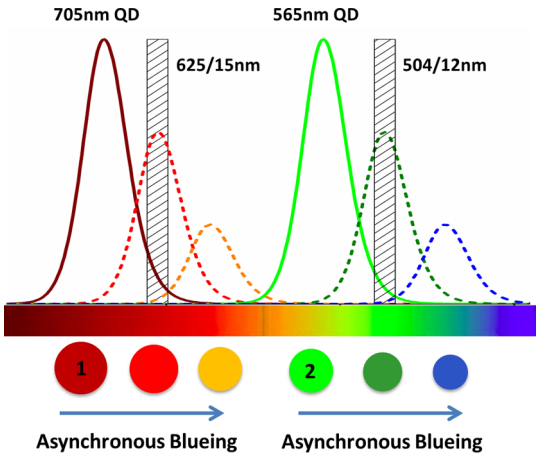

Figure 1. Principle of multicolor blueing. The quantum dots blue shift up to approximately 80 nm, after which the QDs are completely photobleached. The 705 nm QDs will blue and stochastically emit in the 625 nm passband but will no longer emit when they reach the 504 nm passband, which detects the 565 nm QDs. Thus, both colors can be simultaneously detected without cross-talk.

RESULTS AND DISCUSSION

Principle of Two-Color QSTORM. Figure 1 demonstrates the principle of two-color QSTORM. The emission spectra of QDs vary with particle size due to quantum confinement. For core/shell CdSe/ZnS quantum dots, under continuous illumination, the size of the CdSe core shrinks due to the photoinduced oxidation, which results in the shift of the fluorescence emission to shorter wavelengths, a phenomenon known as blueing.[17] As shown in Figure 1, two sizes of CdSe QDs (QD 705 nm and QD 565 nm) are chosen as the probes, and two narrow band-pass filters (625 nm center/15 nm width and 504 nm center/12 nm width) are used to collect the emission from the two QDs, respectively. Due to the asynchronous blueing of the QDs, it is unlikely that multiple QDs within a diffraction-limited area will blue at the same speed and emit in the passband simultaneously.

As has been reported previously, CdSe/ZnS QDs can exhibit blue shifts of as much as 46 nm from their initial emission wavelength.[19] The blueing process is affected by several factors including the laser intensity and the composition of the QD solution, with the concentration of O_2 being especially important.[19,31,32] Under proper conditions, longer blue shifts have been observed. Hoyer *et al.* state that greater than 90% of 705 nm QDs can be detected in a passband between 538 and

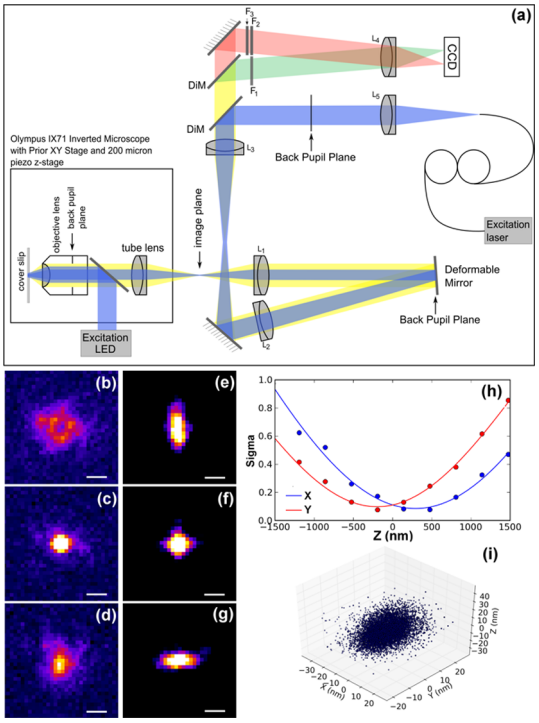

Figure 2. (a) Schematic of the optical setup. L1 and L2 are 350 mm efl achromats. L3 is a 100 mm efl achromat. L4 is a 300 mm efl achromat, and L5 is a 7.86 mm asphere (Thorlabs F240SMA-A). (b–d) Image of a 100 nm fluorescent bead 400 nm above focus, in the focal plane, and 400 nm below focus. (e–g) Images of a 100 nm fluorescent bead 400 nm above focus, in focus, and 400 nm below the focal plane with 0.8 radians of astigmatism added to the PSF with the deformable mirror. (h) Calibration of the astigmatism for three-dimensional STORM; (i) 10 000 localizations of a 100 nm fluorescent bead at 100 fps.

645 nm, indicating a minimum blue shift of 60 nm.[17] Here we measure blueing 705 nm QDs at 625 nm and blueing 565 nm QDs at 504 nm, indicating that QDs can blue shift close to 80 and 61 nm, respectively. (The emission and excitation spectra are shown in Supporting Information Figure S1.)

Optical System. The optical system and performance are shown in Figure 2. The microscope contains a deformable mirror to maintain a Strehl ratio of greater than 0.80, and a home-built optical splitter is used to image both channels on the same CCD camera (Figure 2a). The system PSF is shown in Figure 2b–d. For 3D STORM, astigmatism is used to create an asymmetric PSF (Figure 2e–g).[33] The *z*-position calibration is shown in Figure 2h. Finally, the system stability was tested by imaging a fluorescent microsphere. Over 10 000 images at 100 fps, the standard deviation of position was less than 8 nm in the lateral dimension and less than 12 nm in the axial direction. Further details can be found in the Methods.

Cross-Talk Test. Figure 3 shows measurements of single-color STORM measured with both the green filter and the red filter, indicating that very few localizations are detected in the wrong channel. The 705 nm

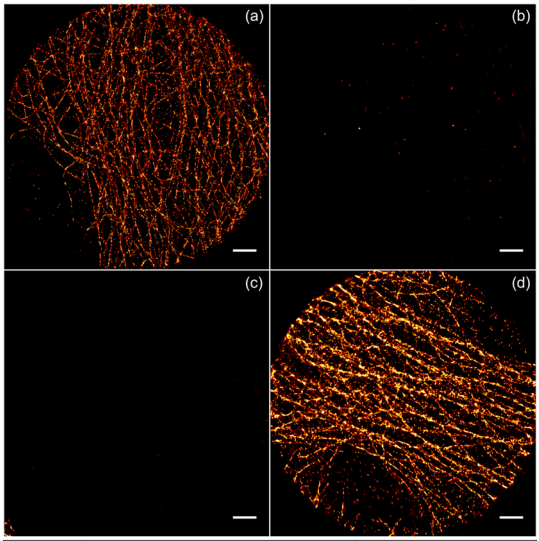

QD type	Number of localizations		Ratio (unwanted/wanted)
	G Channel	*R Channel*	
565	812,227	11,075	0.013635
705	4,836	1,807,726	0.002675

Figure 3. Determination of cross-talk between the two channels. (a,b) STORM measurement of 565 nm QD-labeled microtubules in HepG2 cells. (a) Measurement in the blue channel (504 nm center, 12 nm bandwidth). (b) Measurement in the red channel (625 nm center, 15 nm bandwidth). (c,d) STORM measurement of 705 nm QD-labeled microtubules in HepG2 cells. (c) Measurement in the blue channel. Almost no events are detected. (d) Measurement in the red channel. Scale bars are 2 μm.

QDs are completely oxidized before the emission wavelength of the blueing QDs reaches the 504 nm band-pass filter used to detect the blueing 565 nm QDs. The number of false positives in the blue channel from the 705 nm QDs is less than 0.3% (Figure 3). The number of false positives is higher for the 565 nm QDs in the red channel (1.35%) due to the tail of the unoxidized QDs overlapping the red filter. The majority of these false positives occur within the first 800 frames, so the false positive rate can be reduced by dropping the first frames or simply waiting to start the measurement.

Blueing Speed Optimization. An important aspect of the blueing process for single-molecule localization is the speed of the photo-oxidation. If the molecules blue too quickly, then too many QDs will emit in the pass-band in each exposure; therefore, the likelihood of detecting single QDs in a diffraction-limited area will be too low, and all the QDs will photo-oxidize too quickly, resulting in too few localizations per raw frame. If the QDs blue too slowly, too few single QD emissions will be captured per frame. Then, the experiment will take too long, resulting in too much mechanical drift during the measurements. The resolution of STORM imaging depends on both the photons collected from each QD and the number of localizations.[34] By controlling the blueing rate, both can be improved.

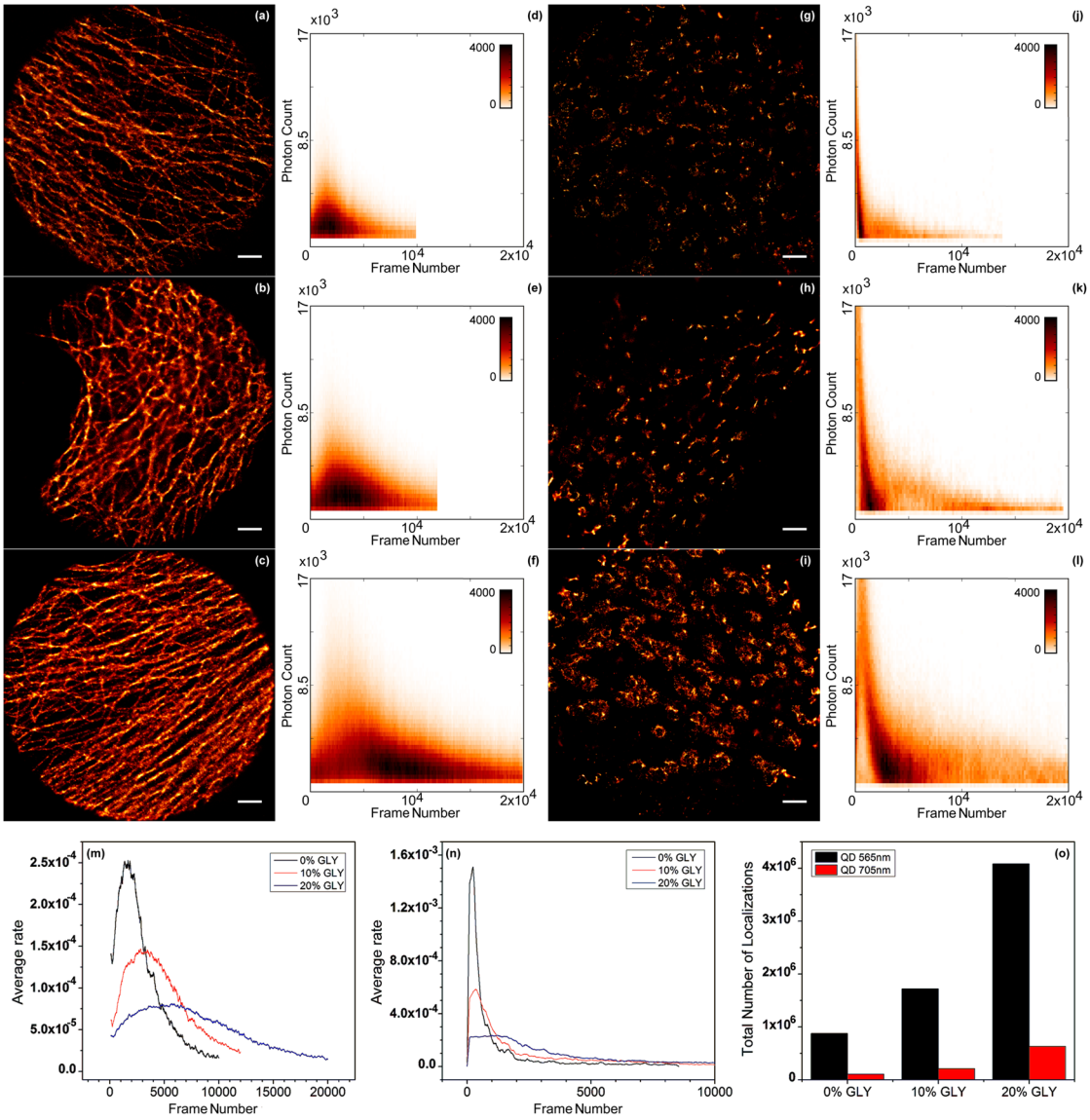

Figure 4. STORM images of microtubules labeled with 565 nm QDs and mitochondria labeled with 705 nm QDs in HepG2 cells in PBS mounting media with 0, 10, and 20% concentrations of glycerol. (a–c) Images of microtubules in 0, 10, and 20% concentrations of glycerol, respectively. (d–f) Plots of average photons per localization (averaged over 100 frames) *vs* frame corresponding to (a–c). Color indicates number of localizations (g–i) images of mitochondria in 0, 10, and 20% concentrations of glycerol, respectively. (j–l) Plots of average photons per localization *vs* frame corresponding to (g–i). The color bar indicates the number of localizations. At least 10 000 frames were collected in total for each experiment at a laser intensity of 3.65 kW/cm^2. Scale bars are 2 μm. (m) Average fraction of total localizations per frame for 565 nm QDs. (n) Average fraction of total localizations per frame for 705 nm QDs. (o) Total number of localizations for different percentages of glycerol.

Here we show that the blueing speed can be optimized by optimizing the laser intensity and the mounting medium. The blueing behavior of QDs mounted in different concentrations of glycerol (0, 10, and 20% v/v) in phosphate-buffered saline (PBS) was characterized. With more glycerol, there is less oxygen available for the photo-oxidation, and the QDs will blue more slowly.

In Figure 4, we show STORM images obtained under the different conditions. In Figure 4a–c, STORM images of microtubules labeled with 565 nm QDs in different concentrations of glycerol are shown. With no glycerol in the mounting medium, there are an insufficient number of localizations (2290 μm^{-2}). The filamentous structure of the microtubules can be seen, but the fidelity of the image is not good, and many of the microtubules are discontinuous. The number of localizations is increased by adding 10% glycerol to the mounting medium (4474 μm^{-2}), and the intact microtubule network can be seen in Figure 4b. Increasing the concentration of glycerol to 20% did not change the microtubule structure significantly. However, for the images of mitochondria that were labeled with 705 nm QDs, the STORM image quality taken with 10% glycerol (Figure 4h) is not good enough to resolve the intact morphology of mitochondria even though it is a

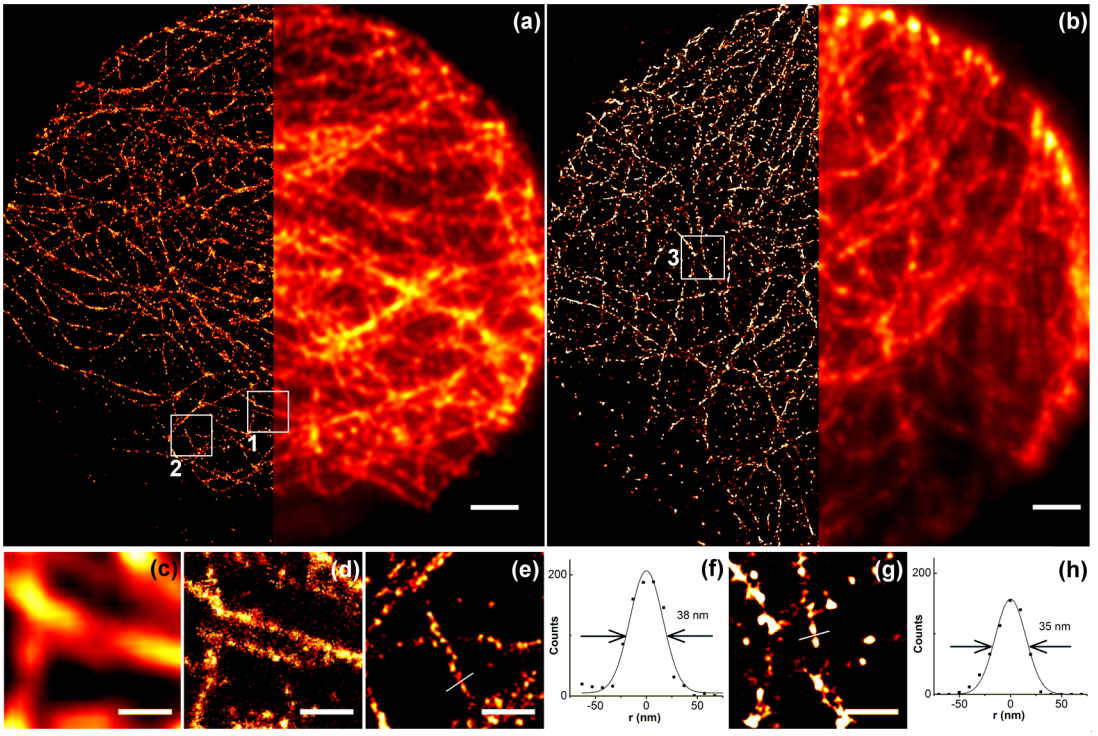

Figure 5. (a,b) STORM (left) and wide-field (right) images of microtubules in HepG2 cells labeled with 565 and 705 nm QDs, respectively. Scale bar is 2 μm. (c,d) Wide-field and STORM images of box 1 in (a). Scale bar is 500 nm. (e) STORM image of box 2 in (a). Scale bar is 500 nm. A cross section of a microtubule is shown in (f). The full width at half-maximum is 38 nm. (g) STORM image of box 3 in (b). Scale bar is 500 nm. A cross section of a microtubule is shown in (h). The full width at half-maximum is 35 nm.

significant improvement over the sample mounted in PBS only (Figure 4g). There are 553 μm^{-2} localizations with 10% glycerol compared to 289 μm^{-2} localizations for PBS only. High-resolution images of mitochondria were obtained with samples mounted in 20% glycerol (Figure 4i), with 1658 μm^{-2} localizations. Increasing the glycerol concentration above 20% did not improve the imaging. With a 50% glycerol concentration, the QDs were still blueing after 50 000 frames at 50 frames per second with many QDs still not having reached the passband. In Figure 4d–f,j–l, we show the average number of photons per localization against frame number for the STORM images in Figure 4a–c,g–i, respectively. With increasing amounts of glycerol, the curve peaks later and spreads out, indicating a slower blueing rate and more localizations at later times. Based on these results, the two-color imaging discussed below was performed on samples mounted in 20% glycerol.

We further analyzed the QD blueing by calculating the ratio of localized QDs per frame to the total number of localizations (Figure 4m,n). This ratio represents an upper bound on the emitting fraction—the number of emitting QDs in a frame to the total number of QDs. Along with photon emission and labeling density, the emitting fraction, *r*, affects the possible resolution. The labeling density must be adjusted to avoid simultaneous emissions within a diffraction-limited area. For higher values of *r*, the labeling density must be lower.[35] We calculate a lower bound on the resolution

$$\Delta x = \sqrt{\pi \left(\frac{\lambda}{2NA}\right)^2 r_{max}}$$

where r_{max} is the maximum emitting fraction over the course of the measurement. Using the data in Figure 4m, we calculate a lower bound on the resolution of 5.5, 4.2, and 3.1 nm for the 565 nm QDs for 0, 10, and 20% concentrations of glycerol in PBS, respectively. For the 705 nm QDs (Figure 4n), we calculate 16.8, 10.4, and 6.6 nm resolution bounds for 0, 10, and 20% concentrations, respectively. The localization software rejects all fluorescent spots that are too large or asymmetric, so the data represent to a high probability only single QD emissions. The total number of localizations in each case is shown in Figure 4o.

Single-Color QSTORM Imaging. In Figure 5, we show single-color STORM images of microtubules stained with 565 and 705 nm QDs. These images show that 565 and 705 nm QDs perform equally well as labels for STORM. In Figure 5c,d, two individual microtubules are clearly separated that cannot be resolved in the wide-field image. From measurements of individual QDs, we determine the lateral resolution to be 24 nm.

A criticism of QD labeling is that the larger size of QDs will limit the achievable resolution due to the

Nyquist sampling criteria.[34] We measure an average microtubule full width at half-maximum of 60 ± 12 nm from QSTORM images by performing Gaussian fits to the cross section of 12 microtubules averaged over ~500 nm of length, as shown in Figure S5. The best images produce a width of 46 nm. This is slightly larger than previous measurements of the microtubule width from STORM imaging,[17,36] indicating that the QD size increases the effective width by ~10 nm. The microtubule diameter is 25 nm as determined by transmission electron microscopy.[37] The size of the quantum dots is only a few nanometers, but coatings for biocompatibility and functionalization are usually required for biology applications, which will increase the final labeling size to ~20 nm, and the size of a typical IgG antibody is about 7 nm.[38] Considering the size of primary antibodies and QD-labeled secondary antibodies on either side of the microtubule, our measurements match the size of the labeled microtubule. By labeling microtubules using nanobodies, the diameter of the microtubule has been measured as 26.9 ± 3.7 nm with single-molecule nanoscopy.[39]

Compared to organic dyes, QDs show remarkable photostability and brightness. Even though the intensity decreases during the blueing process, they still emit a large number of photons before being bleached. We compared QSTORM to STORM with Alexa 647 (Figure S2), which is considered one of the most efficient cyanine dye labels for STORM imaging.[40] The cyanine dyes can be turned on and off reliably for hundreds of cycles before photobleaching, and the size of the dye molecule is very small, allowing high-resolution STORM imaging.[6,41] For QD blueing, each QD is detected only once, but due to the high quantum yield, many photons can still be collected. Figure S2 shows the histograms of photon counts for the two QDs and Alexa 647. Comparing histograms of the Alexa 647 with the 565 and 705 nm QDs, we can see that there are more photons emitted from the QDs. Accurate localizations by the large photon number is a major advantage of QSTORM imaging over other stochastic approaches using organic dyes or fluorescent proteins. The large photon count is even more important for obtaining high resolution in the presence of background fluorescence (from autofluorescence or out-of-focus fluorescence in thick samples) because the background degrades the resolution.[8]

Multicolor QSTORM Imaging. STORM imaging of mitochondria and microtubules has been previously reported with a number of different probes.[22,28,35] In Huang *et al.*,[28] TOM20 in the mitochondria outer membrane was labeled with a photoswitchable probe consisting of A405 linked to Cy5. In Shim *et al.*,[22] Mitotracker dyes are used to label the mitochondria inner membrane. In van de Linde *et al.*,[35] F_0F_1-ATP-synthase and cytochrome *c* oxidase are stained with Alexa 647. The antibody MTC02 recognizes a 60 kDa nonglycosylated protein component of mitochondria found in human cells and has been used for mitochondrial content determination or mitochondria imaging in a variety of previous studies.[42−44] Here we use this antibody for STORM imaging to demonstrate the morphology of mitochondria as well as their relationship with microtubules.

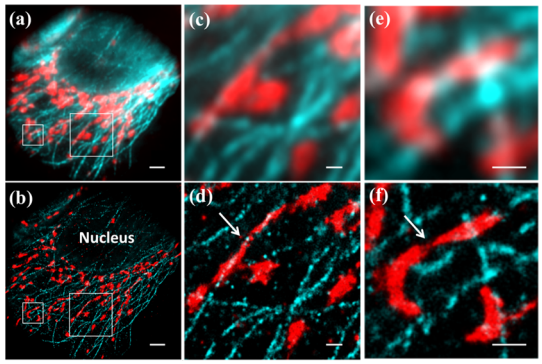

Figure 6. Two-color STORM images of QD565 microtubules (blue) and QD705 mitochondria (red). (a,b) Wide-field and STORM images, respectively. Scale bars are 2 μm. (c,d) Magnified images of the boxed region on the right in (a) and (b). Scale bars are 500 nm. (e,f) Magnified images of the boxed region on the left in (a) and (b). Scale bars are 500 nm.

Figure 6 shows multicolor wide-field and STORM images presented at different scales. Compared to the wide-field image, the STORM image provides more detail of the structure of both the microtubules and the mitochondria as well as their relationship. The distribution and morphology of the mitochondria are also demonstrated in the STORM images. As can be seen in Figure 6, the mitochondrial distribution is heterogeneous, much denser near the nucleus where the energy requirement is higher.[45] Furthermore, heterogeneous mitochondrial morphologies—elongated, tubular and short, globular—are observed. Most of the mitochondria, but not all, are in contact with and aligned along the microtubules, consistent with the fact that mitochondria are predominantly transported along the microtubule network in mammalian cells.[46,47] The tubular mitochondria are often aligned along the microtubules (Figure 6d), but it has also been reported that sometimes such connections between the mitochondria and microtubule are noncontiguous, and such inchworm-like contact is considered to aid transport.[28,47] Mitochondria are highly dynamic organelles that often change morphology; fusion and fission of mitochondria have been imaged over time by live confocal microscopy[48] as well as live STORM imaging.[22] In our work, we also observed that two mitochondrial compartments could be connected by a thin, extended tubular structure (Figure 6f). Such tubular intermediates are not clearly resolved in the wide-field images.

Multicolor 3D QSTORM Imaging by Astigmatism. We have also extended two-color QSTORM to three-dimensional

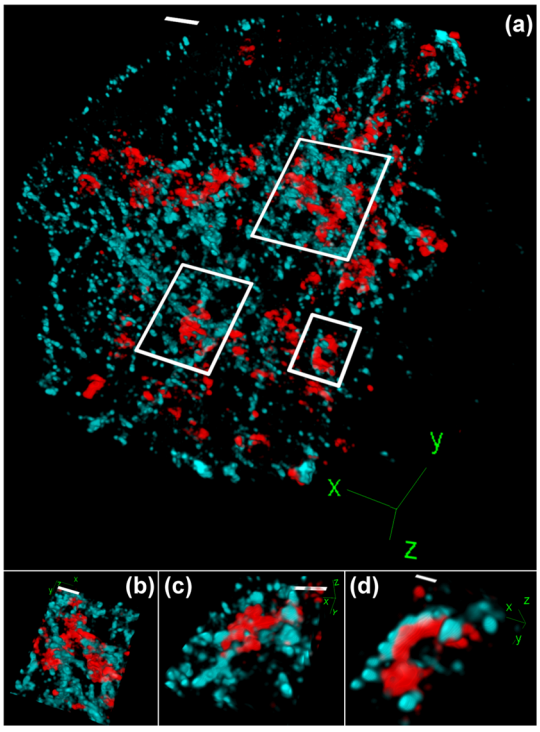

Figure 7. Three-dimensional STORM images of microtubules (blue) and mitochondria (red) in HepG2 cells. (a) Large field of view. Scale bar is 2 μm. (b–d) Close-up images of the boxed regions in (a). Scale bars are 500 nm.

imaging by applying astigmatism to the deformable mirror to create an astigmatic PSF.[33,49] The results are shown in Figure 7. These images clearly show the three-dimensional arrangement of the microtubules and mitochondria, although the number of localizations is reduced compared to 2D STORM because of the larger astigmatic PSF. The 3D images give more details of the spatial relationship between the mitochondria and microtubules, which can be obscured in conventional or 2D STORM images. It can be clearly seen in the 3D images that the microtubule and mitochondrial networks are strongly interwoven with each other, and the mitochondria can be tightly wrapped around the microtubules rather than just attached to them. The interwoven structure between mitochondria and microtubules has also been observed by 4Pi microscopy using QD staining.[13]

CONCLUSION

In conclusion, we have demonstrated that superresolution imaging with quantum dots can be extended to multiple colors without sacrificing resolution. We demonstrate that the quantum dot blueing process can be controlled to maximize the number of achievable localizations, and we report careful measurements of the microtubule width measured with QSTORM and demonstrate that indeed higher photon counts can be achieved with quantum dots.

Here we have demonstrated multicolor QSTORM using two QDs that are far apart in initial wavelength, allowing us to completely separate the blueing emission into separate channels. Future work will focus on extending QSTORM to more than two colors and to thicker samples.

METHODS

Materials and Solution Preparation. HepG2 cells and Eagle's minimum essential medium (EMEM) were purchased from ATCC. Bovine serum albumin (BSA) was purchased from Santa Cruz Biotechnology Inc. Anti-alpha tubulin rabbit primary antibody and anti-mitochondria MTC02 mouse primary antibody were purchased from abcam. Fetal bovine serum (FBS), normal goat serum (10%), Qdot 565 goat F(ab′)2 anti-rabbit IgG conjugate (H+L), Qdot 705 goat F(ab′)2 anti-mouse IgG conjugate (H+L), Alexa Fluor 647 goat anti-rabbit IgG (H+L) antibody, Alexa Fluor 488 goat anti-mouse IgG (H+L) antibody, and TetraSpeck microspheres (0.1 μm diameter, blue/green/orange/dark red fluorescence) were purchased from Life Technologies. Anti-alpha tubulin mouse primary antibody, cysteamine (MEA), glucose oxidase, and catalase were purchased from Sigma-Aldrich.

Buffers were prepared as follows:

1. Blocking buffer: 6% BSA + 10% normal serum in PBS.
2. Washing buffer: 0.2% BSA + 0.05% Triton X-100 in PBS.
3. Antibody incubation buffer: 6% BSA in PBS.
4. STORM imaging buffer for Alexa 647 and Alexa 488 was prepared according to the Nikon N-STORM protocol; 50 mM Tris-HCl pH 8.0, 10 mM NaCl, 0.1 M MEA, 10% w/v glucose, 0.56 mg/mL glucose oxidase, 0.17 mg/mL catalase.

Cell Culture and Immunostaining. HepG2 cells were cultured in ATCC-formulated EMEM with 10% FBS. The cells were plated onto a PLL (poly-L-lysine)-coated glass-bottom dish at an initial confluency of about 50% and cultured for 1 day to let the cells attach to the dish.

To immunostain, the culture medium was aspirated, and the cells were washed with PBS once and fixed in a 1:1 acetone/methanol solution for 10 min. After three washes with PBS, the cells were blocked by incubation with blocking buffer for 2 h. Then the blocking buffer was aspirated, and the cells were incubated with one or both primary antibodies diluted in 6% BSA at 4 °C overnight. Then the cells were washed three times with the washing buffer for 10 min per wash. Then the corresponding secondary antibodies labeled with quantum dots or Alexa Fluor were added to the sample in 6% BSA and incubated for 2 h, protected from light. The cells were washed again three times with washing buffer and one time with PBS for 10 min per wash and stored in PBS before imaging. Immediately before imaging, the buffer was switched either to the glycerol solution in PBS for QD labeling or to the STORM imaging buffer for Alexa Fluor labeling.

Optical Setup and Data Acquisition. Imaging data were acquired using an Olympus IX71 inverted microscope with a 60× oil objective (Plan Apo N). The microscope was equipped with a PriorProScan *xy* stage and a Prior NanoScanZ piezo stage for focusing. Fluorescence was imaged using an Andor EMCCD camera (DV887DCS-BV with 14 bit ADC). At the left-side port of the IX71, additional optics were inserted to reimage the back pupil plane of the objective onto a deformable mirror (Mirao 52E, Imagine Optic). The diameter of the deformable mirror limits the system NA to 1.28. After the deformable mirror, a further image plane is generated, which is then relayed to the CCD camera with an additional 3× magnification so that

the image is sampled at the Nyquist frequency by the CCD. A CCD pixel corresponds to 89 nm at the sample plane.

A dichroic mirror separated the red and green channels (Omega XF2054). One filter detects the blueing 565 nm QDs (Semrock 504/12 nm), and a second filter detects the blueing 705 nm QDs (Semrock 625/15 nm). A 0.6 OD neutral density filter (Thorlabs ND06A) was added to the red channel to compensate for the higher brightness of the 705 nm QDs.

The QDs were excited with a 488 nm laser (Cyan 488, Newport) which was coupled into a 100 μm core diameter fiber. The fiber was shaken using a fiber shaker to remove speckle.[50] To excite Alexa Fluor 647, a 660 nm laser (Obis 660LX, Coherent) was coupled into a separate fiber attached to the shaker.

Adaptive Optics. Although the measurements described in this paper do not use active adaptive optics to correct aberrations for each sample, AO was used to maintain a Strehl ratio of greater than 0.7 using phase retrieval[51] and to introduce to astigmatism into the optical path for 3D STORM.[49]

Image Processing. STORM images were generated using RapidSTORM software (version 2.21 or version 3.2). The 3D images in Figure 7 were generated using ImageJ.

Blueing Rate Test. The blueing rate (Figure 4) was tested on microtubules stained with 565 nm QDs and mitochondria stained with 705 nm QDs in HepG2 cells with three mounting media: 100% PBS, 90% PBS and 10% glycerol, and 80% PBS and 20% glycerol. All tests were performed sequentially on one sample; after new mounting medium was added, the medium was allowed to settle for 10 min before the next experiment.

Conflict of Interest: The authors declare no competing financial interest.

Supporting Information Available: Optical spectra of antibody-conjugated quantum dots. Comparison of QDs and Alexa dyes; measurement of resolution; details of chromatic calibration; calculations of microtubule width; STORM images of mitochondria labeled with Alexa 488; measurement of blueing efficiency. This material is available free of charge *via* the Internet at http://pubs.acs.org.

Acknowledgment. This work was supported by Grant MCB1052672 from the National Science Foundation. We would like to thank Drs. W. Kisaalita and A. Asthana for providing assistance with cell culture.

REFERENCES AND NOTES

1. Hell, S. W. Far-Field Optical Nanoscopy. *Science* **2007**, *316*, 1153–1158.
2. Huang, B.; Babcock, H.; Zhuang, X. Breaking the Diffraction Barrier: Super-resolution Imaging of Cells. *Cell* **2010**, *143*, 1047–1058.
3. Hell, S. W.; Wichmann, J. Breaking the Diffraction Resolution Limit by Stimulated Emission: Stimulated-Emission-Depletion Fluorescence Microscopy. *Opt. Lett.* **1994**, *19*, 780–782.
4. Klar, T. A.; Hell, S. W. Subdiffraction Resolution in Far-Field Fluorescence Microscopy. *Opt. Lett.* **1999**, *24*, 954–956.
5. Gustafsson, M. G. Surpassing the Lateral Resolution Limit by a Factor of Two Using Structured Illumination Microscopy. *J. Microsc.* **2000**, *198*, 82–87.
6. Rust, M. J.; Bates, M.; Zhuang, X. Sub-diffraction-Limit Imaging by Stochastic Optical Reconstruction Microscopy (STORM). *Nat. Methods* **2006**, *3*, 793–796.
7. Betzig, E.; Patterson, G. H.; Sougrat, R.; Lindwasser, O. W.; Olenych, S.; Bonifacino, J. S.; Davidson, M. W.; Lippincott-Schwartz, J.; Hess, H. F. Imaging Intracellular Fluorescent Proteins at Nanometer Resolution. *Science* **2006**, *313*, 1642–1645.
8. Thompson, R. E.; Larson, D. R.; Webb, W. W. Precise Nanometer Localization Analysis for Individual Fluorescent Probes. *Biophys. J.* **2002**, *82*, 2775–2783.
9. Chan, W. C. W.; Nie, S. Quantum Dot Bioconjugates for Ultrasensitive Nonisotopic Detection. *Science* **1998**, *281*, 2016–2018.
10. Bruchez, M.; Moronne, M.; Gin, P.; Weiss, S.; Alivisatos, A. P. Semiconductor Nanocrystals as Fluorescent Biological Labels. *Science* **1998**, *281*, 2013–2016.
11. Resch-Genger, U.; Grabolle, M.; Cavaliere-Jaricot, S.; Nitschke, R.; Nann, T. Quantum Dots *versus* Organic Dyes as Fluorescent Labels. *Nat. Methods* **2008**, *5*, 763–775.
12. Irvine, S.; Staudt, T.; Rittweger, E.; Engelhardt, J.; Hell, S. Direct Light-Driven Modulation of Luminescence from Mn-Doped ZnSe Quantum Dots. *Angew. Chem., Int. Ed.* **2008**, *47*, 2685–2688.
13. Medda, R.; Jakobs, S.; Hell, S. W.; Bewersdorf, J. 4Pi Microscopy of Quantum Dot-Labeled Cellular Structures. *J. Struct. Biol.* **2006**, *156*, 517–523.
14. Dertinger, T.; Colyer, R.; Iyer, G.; Weiss, S.; Enderlein, J. Fast, Background-Free, 3D Super-resolution Optical Fluctuation Imaging (SOFI). *Proc. Natl. Acad. Sci. U.S.A.* **2009**, *106*, 22287–22292.
15. Watanabe, T. M.; Fukui, S.; Jin, T.; Fujii, F.; Yanagida, T. Real-Time Nanoscopy by Using Blinking Enhanced Quantum Dots. *Biophys. J.* **2010**, *99*, L50–L52.
16. Wang, Y.; Fruhwirth, G.; Cai, E.; Ng, T.; Selvin, P. R. 3D Super-resolution Imaging with Blinking Quantum Dots. *Nano Lett.* **2013**, *13*, 5233–5241.
17. Hoyer, P.; Staudt, T.; Engelhardt, J.; Hell, S. W. Quantum Dot Blueing and Blinking Enables Fluorescence Nanoscopy. *Nano Lett.* **2010**, *11*, 245–250.
18. Nirmal, M.; Dabbousi, B. O.; Bawendi, M. G.; Macklin, J. J.; Trautman, J. K.; Harris, T. D.; Brus, L. E. Fluorescence Intermittency in Single Cadmium Selenide Nanocrystals. *Nature* **1996**, *383*, 802–802.
19. van Sark, W. G. J. H. M.; Frederix, P. L. T. M.; Bol, A. A.; Gerritsen, H. C.; Meijerink, A. Blueing, Bleaching, and Blinking of Single CdSe/ZnS Quantum Dots. *ChemPhysChem* **2002**, *3*, 871–879.
20. Cordero, S. R.; Carson, P. J.; Estabrook, R. A.; Strouse, G. F.; Buratto, S. K. Photo-activated Luminescence of CdSe Quantum Dot Monolayers. *J. Phys. Chem. B* **2000**, *104*, 12137–12142.
21. van Sark, W. G. J. H. M.; Frederix, P. L. T. M.; Van den Heuvel, D. J.; Gerritsen, H. C.; Bol, A. A.; van Lingen, J. N. J.; de Mello Donegá, C.; Meijerink, A. Photooxidation and Photobleaching of Single CdSe/ZnS Quantum Dots Probed by Room-Temperature Time-Resolved Spectroscopy. *J. Phys. Chem. B* **2001**, *105*, 8281–8284.
22. Shim, S.-H.; Xia, C.; Zhong, G.; Babcock, H. P.; Vaughan, J. C.; Huang, B.; Wang, X.; Xu, C.; Bi, G.-Q.; Zhuang, X. Super-resolution Fluorescence Imaging of Organelles in Live Cells with Photoswitchable Membrane Probes. *Proc. Natl. Acad. Sci. U.S.A.* **2012**, *109*, 13978–13983.
23. Schermelleh, L.; Carlton, P. M.; Haase, S.; Shao, L.; Winoto, L.; Kner, P.; Burke, B.; Cardoso, M. C.; Agard, D. A.; Gustafsson, M. G. L.; et al. Subdiffraction Multicolor Imaging of the Nuclear Periphery with 3D Structured Illumination Microscopy. *Science* **2008**, *320*, 1332–1336.
24. Schmidt, R.; Wurm, C. A.; Jakobs, S.; Engelhardt, J.; Egner, A.; Hell, S. W. Spherical Nanosized Focal Spot Unravels the Interior of Cells. *Nat. Methods* **2008**, *5*, 539–544.
25. Bock, H.; Geisler, C.; Wurm, C. A.; von Middendorff, C.; Jakobs, S.; Schönle, A.; Egner, A.; Hell, S. W.; Eggeling, C. Two-Color Far-Field Fluorescence Nanoscopy Based on Photoswitchable Emitters. *Appl. Phys. B: Lasers Opt.* **2007**, *88*, 161–165.
26. Shroff, H.; Galbraith, C. G.; Galbraith, J. A.; White, H.; Gillette, J.; Olenych, S.; Davidson, M. W.; Betzig, E. Dual-Color Superresolution Imaging of Genetically Expressed Probes within Individual Adhesion Complexes. *Proc. Natl. Acad. Sci. U.S.A.* **2007**, *104*, 20308–20313.
27. Bates, M.; Huang, B.; Dempsey, G. T.; Zhuang, X. Multicolor Super-resolution Imaging with Photo-switchable Fluorescent Probes. *Science* **2007**, *317*, 1749–1753.
28. Huang, B.; Jones, S. A.; Brandenburg, B.; Zhuang, X. Whole-Cell 3D STORM Reveals Interactions between Cellular Structures with Nanometer-Scale Resolution. *Nat. Methods* **2008**, *5*, 1047–1052.
29. Cutler, P. J.; Malik, M. D.; Liu, S.; Byars, J. M.; Lidke, D. S.; Lidke, K. A. Multi-color Quantum Dot Tracking Using a

High-Speed Hyperspectral Line-Scanning Microscope. *PLoS One* **2013**, *8*, e64320.
30. Clausen, M. P.; Arnspang, E. C.; Ballou, B.; Bear, J. E.; Lagerholm, B. C. Simultaneous Multi-species Tracking in Live Cells with Quantum Dot Conjugates. *PLoS One* **2014**, *9*, e97671.
31. Shi, X.; Meng, X.; Sun, L.; Liu, J.; Zheng, J.; Gai, H.; Yang, R.; Yeung, E. S. Observing Photophysical Properties of Quantum Dots in Air at the Single Molecule Level: Advantages in Microarray Applications. *Lab Chip* **2010**, *10*, 2844–2847.
32. Chen, H.; Gai, H.; Yeung, E. S. Inhibition of Photobleaching and Blue Shift in Quantum Dots. *Chem. Commun.* **2009**, 1676–1678.
33. Huang, B.; Wang, W.; Bates, M.; Zhuang, X. Three-Dimensional Super-resolution Imaging by Stochastic Optical Reconstruction Microscopy. *Science* **2008**, *319*, 810–813.
34. Shroff, H.; Galbraith, C. G.; Galbraith, J. A.; Betzig, E. Live-Cell Photoactivated Localization Microscopy of Nanoscale Adhesion Dynamics. *Nat. Methods* **2008**, *5*, 417–423.
35. van de Linde, S.; Wolter, S.; Heilemann, M.; Sauer, M. The Effect of Photoswitching Kinetics and Labeling Densities on Super-resolution Fluorescence Imaging. *J. Biotechnol.* **2010**, *149*, 260–266.
36. Heilemann, M.; van de Linde, S.; Schüttpelz, M.; Kasper, R.; Seefeldt, B.; Mukherjee, A.; Tinnefeld, P.; Sauer, M. Subdiffraction-Resolution Fluorescence Imaging with Conventional Fluorescent Probes. *Angew. Chem., Int. Ed.* **2008**, *47*, 6172–6176.
37. Weber, K.; Rathke, P. C.; Osborn, M. Cytoplasmic Microtubular Images in Glutaraldehyde-Fixed Tissue Culture Cells by Electron Microscopy and by Immunofluorescence Microscopy. *Proc. Natl. Acad. Sci. U.S.A.* **1978**, *75*, 1820–1824.
38. Heilemann, M.; van de Linde, S.; Mukherjee, A.; Sauer, M. Super-resolution Imaging with Small Organic Fluorophores. *Angew. Chem., Int. Ed.* **2009**, *48*, 6903–6908.
39. Ries, J.; Kaplan, C.; Platonova, E.; Eghlidi, H.; Ewers, H. A Simple, Versatile Method for GFP-Based Super-resolution Microscopy *via* Nanobodies. *Nat. Methods* **2012**, *9*, 582–584.
40. Dempsey, G. T.; Vaughan, J. C.; Chen, K. H.; Bates, M.; Zhuang, X. Evaluation of Fluorophores for Optimal Performance in Localization-Based Super-resolution Imaging. *Nat. Methods* **2011**, *8*, 1027–1036.
41. Dempsey, G. T.; Bates, M.; Kowtoniuk, W. E.; Liu, D. R.; Tsien, R. Y.; Zhuang, X. Photoswitching Mechanism of Cyanine Dyes. *J. Am. Chem. Soc.* **2009**, *131*, 18192–18193.
42. Geyer, F. C.; de Biase, D.; Lambros, M. B.; Ragazzi, M.; Lopez-Garcia, M. A.; Natrajan, R.; Mackay, A.; Kurelac, I.; Gasparre, G.; Ashworth, A.; et al. Genomic Profiling of Mitochondrion-Rich Breast Carcinoma: Chromosomal Changes May Be Relevant for Mitochondria Accumulation and Tumour Biology. *Breast Cancer Res. Treat.* **2012**, *132*, 15–28.
43. Grupp, K.; Jedrzejewska, K.; Tsourlakis, M. C.; Koop, C.; Wilczak, W.; Adam, M.; Quaas, A.; Sauter, G.; Simon, R.; Izbicki, J. R.; et al. High Mitochondria Content Is Associated with Prostate Cancer Disease Progression. *Mol. Cancer* **2013**, *12*, 145.
44. Hall, C. J.; Boyle, R. H.; Sun, X.; Wicker, S. M.; Misa, J. P.; Krissansen, G. W.; Print, C. G.; Crosier, K. E.; Crosier, P. S. Epidermal Cells Help Coordinate Leukocyte Migration during Inflammation through Fatty Acid-Fuelled Matrix Metalloproteinase Production. *Nat. Commun.* **2014**, *5*, 3880.
45. Li, Z.; Okamoto, K.; Hayashi, Y.; Sheng, M. The Importance of Dendritic Mitochondria in the Morphogenesis and Plasticity of Spines and Synapses. *Cell* **2004**, *119*, 873–887.
46. Saxton, W. M.; Hollenbeck, P. J. The Axonal Transport of Mitochondria. *J. Cell Sci.* **2012**, *125*, 2095–2104.
47. Boldogh, I. R.; Pon, L. A. Mitochondria on the Move. *Trends Cell Biol.* **2007**, *17*, 502–510.
48. Karbowski, M.; Youle, R. J. Dynamics of Mitochondrial Morphology in Healthy Cells and During Apoptosis. *Cell Death Differ.* **2003**, *10*, 870–880.
49. Izeddin, I.; El Beheiry, M.; Andilla, J.; Ciepielewski, D.; Darzacq, X.; Dahan, M. PSF Shaping Using Adaptive Optics for Three-Dimensional Single-Molecule Super-resolution Imaging and Tracking. *Opt. Express* **2012**, *20*, 4957–4967.
50. Shao, L.; Kner, P.; Rego, E. H.; Gustafsson, M. G. Super-resolution 3D Microscopy of Live Whole Cells Using Structured Illumination. *Nat. Methods* **2011**, *8*, 1044–1046.
51. Kner, P.; Winoto, L.; Agard, D. A.; Sedat, J. W. Closed Loop Adaptive Optics for Microscopy without a Wavefront Sensor. *Proc. SPIE* **2010**, *7570*, 757006–757009.